Pico-phytoplankton contribute half of global marine carbon export

Robert T. Letscher[1,2], J. Keith Moore[3], Adam C. Martiny[3,4], Michael W. Lomas[5]

[1]Ocean Process Analysis Laboratory, University of New Hampshire, Durham, NH, USA

[2]Earth Sciences, University of New Hampshire, Durham, NH, USA

[3]Earth System Science, University of California, Irvine, CA, USA

[4]Ecology and Evolutionary Biology, University of California, Irvine, CA, USA

[5]Bigelow Laboratory for Ocean Sciences, East Boothbay, ME, USA

Corresponding author: Robert Letscher (robert.letscher@unh.edu)

Key Points:

- Explicitly simulated *Prochlorococcus*, *Synechococcus*, and pico-eukaryotes contribute ~60% of global net primary productivity
- Pico-phytoplankton contribute half of global marine sinking particle export production
- Carbon export is elevated poleward of western boundary currents, dominated by pico-eukaryotes and diatoms with elevated C:P stoichiometry

Abstract

Earth System Models generally predict increasing upper ocean stratification from 21st century planetary warming, which will cause a decrease in the vertical nutrient flux resulting in declining marine net primary productivity (NPP) and carbon export fluxes. Recent advances in quantifying marine ecosystem carbon to nutrient stoichiometry have identified large latitudinal and biome variability, with low-latitude oligotrophic systems harboring pico-sized phytoplankton exhibiting large phosphorus to carbon cellular plasticity. Climate forced changes in nutrient flux stoichiometry and phytoplankton community composition is thus likely to alter the ocean's biogeochemical response and feedback with the carbon-climate system. We have added three pico-phytoplankton functional types within the Biogeochemical Elemental Cycling component of the Community Earth System Model while incorporating variable cellular phosphorus to carbon stoichiometry for all represented phytoplankton types. The model simulates *Prochlorococcus* and *Synechococcus* populations that dominate the productivity and sinking carbon export of the tropical and subtropical ocean, and pico-eukaryote populations that contribute significantly to productivity and export within the subtropical to mid-latitude transition zone, contributing a combined 50 – 70% of these fluxes. Pico-phytoplankton cellular stoichiometry and resulting sinking export patterns inversely track the distribution of surface phosphate, with the western subtropical regions of each basin supporting the most P-poor stoichiometries. Collectively, pico-phytoplankton contribute ~58% of global NPP and ~46% of global particulate organic carbon export below 100 meters. Subtropical gyre recirculation regions along the poleward flanks of surface western boundary currents are identified as regional hotspots of enhanced carbon export exhibiting C-rich/P-poor stoichiometry, preferentially inhabited by pico-eukaryotes and diatoms.

1. **Introduction**

Ocean biogeochemical (OBGC) models operating within larger Earth System Models (ESMs) have been developed for the purpose of quantifying the feedbacks between ocean biology, chemistry, and the climate system as well as to provide predictions of ocean biogeochemistry fluxes and tracer concentrations decades to centuries into the future (Le Quéré et al., 2005; Friedlingstein et al., 2006; Bopp et al., 2013; Cabré et al., 2015; Moore et al., 2013; 2018). ESM output from the Coupled Model Intercomparison Project Phase 5 (CMIP5) and Phase 6 (CMIP6) has predicted ocean acidification, deoxygenation, and decreasing primary productivity during the 21st century (Bopp et al., 2013; Cabré et al., 2015, Moore et al., 2013; Kwiatkowski et al., 2020) and beyond (Moore et al., 2018) under a business-as-usual scenario, primarily as a result of changes in ocean circulation and stratification in response to warming ocean temperatures. Enhanced upper ocean stratification leads to a reduction in vertical nutrient flux to the sunlight surface layer, decreasing net primary productivity (NPP) by phytoplankton, with a concomitant reduction in carbon export to the ocean interior (Cabré et al., 2015; Wilson et al., 2022), resulting in a positive feedback with the climate system as ocean carbon uptake is diminished with sustained warming. These declines are nearly universal among CMIP5 models, most of which feature fixed C:N:P:-O_2 stoichiometry (i.e. the Redfield ratio; Redfield et al., 1934; 1958) to describe phytoplankton nutrient uptake, production of organic matter, and its subsequent remineralization (Bopp et al., 2013). Further, declines in key carbon cycle features persist in the latest generation CMIP6 models despite an increasingly prevalent switch to variable nutrient to carbon quotas within the marine biogeochemistry modules (Séférian et al., 2020; Wilson et al., 2022).

Common to nearly all OBGC models is the representation of one or more 'groups' of phytoplankton that consume inorganic nutrients, resulting in photosynthesis, net primary production, and production of autotrophic biomass. Autotrophy is most often distributed among ≥ 2 phytoplankton functional types (PFTs), that are chosen to represent differing growth strategies, e.g., slower-growing small pico- and nano-phytoplankton vs. fast-growing large diatoms, to capture biogeographic latitudinal trends in nutrient uptake rates, cell size, and export efficiency. Phytoplankton growth experiences top-down control due to grazing by one or more zooplankton groups, also resulting in the production of particulate and dissolved organic detrital pools. Bottom-up controls on phytoplankton growth include multiple nutrient limitations, light limitation, and optimum temperature effects. Generally, nutrient uptake affinity is inversely correlated with cell size with smaller PFTs better able to acquire nutrients at low *in situ* concentrations. Each PFT acquires nutrients to satisfy their particular cellular N:C, P:C, and/or Fe:C quota, depending on the simulated inorganic nutrient fields. These cellular nutrient quotas are invariant for fixed stoichiometry models (i.e., at Redfield proportions; Moore et al., 2004; Dunne et al., 2010; Ilyina et al., 2013; Aumont et al., 2015) or can be variable, dependent on *in situ* environmental parameters such as nutrient concentration (Galbraith & Martiny, 2015) or optimal resource allocation theory describing phytoplankton cellular functions (Klausmeier et al., 2004; Dunne, 2013; Kwiatkowski et al., 2018). Many culture and field observations have documented variability in cellular nutrient quotas that vary both with ambient nutrient concentrations (Tanioka et al., 2022; Karl et al., 2001; Rhee, 1978) and/or across PFTs (Martiny et al., 2013a; Baer et al., 2017; Geider & La Roche, 2002; Quigg et al., 2003). Additionally, with the emergence of flow cytometry for the study of marine microbes (Lomas et al., 2011), a large literature of field and culture based studies has accumulated in recent decades describing the

92 physiology, biogeography, and phylogeny of marine pico-phytoplankton, more specifically the
93 cyanobacterial lineages *Prochlorococcus* and *Synechococcus* and pico-eukaryotic phytoplankton,
94 which now allows for their representation in numerical marine ecosystem models (e.g. Moore et
95 al., 1998; Partensky et al., 1998; DuRand et al., 2001; Martiny et al., 2009; Buitenhuis et al.,
96 2012; Pasulka et al., 2013; Flombaum et al., 2013; 2020; Sohm et al., 2016; Baer et al., 2017).
97 Given the need to balance model complexity against limiting computational resources,
98 representation of additional pico-phytoplankton groups is perhaps of first order importance with
99 respect to introduction of variable elemental stoichiometry within OBGC models, since pico-
100 phytoplankton are known to exhibit the largest carbon to nutrient cellular plasticity (Quigg et al.,
101 2003; Klausmeier et al., 2004; Martiny et al., 2013a; Baer et al., 2017). In light of these
102 advances, representing the pico-phytoplankton and variable carbon to nutrient content of all
103 phytoplankton in OBGC models has become a pressing goal to better capture the ocean
104 ecosystem response to the changing 21st century climate and its associated feedbacks with the
105 climate system.

106 Many recent studies have identified and quantified the non-Redfield, variable carbon to
107 nutrient stoichiometry that permeates most ocean biogeochemical fluxes and tracer pools
108 including dissolved nutrients (Weber & Deutsch, 2010), biomass (Tanioka & Matsumoto, 2020),
109 particulate organic matter (Martiny et al., 2013a), dissolved organic matter (Letscher & Moore,
110 2015), export production (Teng et al., 2014), and organic matter remineralization (DeVries &
111 Deutsch, 2014). The emergent pattern from these studies is one of carbon-rich (nutrient-poor)
112 stoichiometry that describes biogeochemical functioning in the lower latitude, nutrient-poor
113 biomes of the subtropics, while the nutrient-replete upwelling and subpolar biomes exhibit
114 stoichiometries at or slightly below Redfield carbon to nutrient proportions. Two mechanisms

have been suggested to contribute to the observed biogeography of marine ecosystem stoichiometry including phosphorus and/or nitrogen plasticity by the extant phytoplankton community (e.g. Galbraith & Martiny, 2015; Van Mooy et al., 2009) as well as shifts in phytoplankton community composition across biomes with relatively nutrient-deficient cyanobacteria dominating the subtropics and more nutrient-rich diatoms and other larger phytoplankton dominating elsewhere (e.g. Arrigo et al., 1999; Weber & Deutsch, 2010; Sharoni & Halevy, 2020). Cell-sorted field populations of cyanobacteria (*Prochlorococcus* and *Synechococcus*) and pico-eukaryotes from the Sargasso Sea, eastern Pacific, and Indian Ocean suggest both mechanisms may be at play as cyanobacteria exhibited lower cellular P content as compared to eukaryotes, while all groups exhibited cellular P plasticity in response to latitudinal gradients in inorganic phosphorus availability, albeit at varying degrees across taxonomic groups (Martiny et al., 2013a; Baer et al., 2017; Lomas et al., 2021).

Does representation of variable carbon to nutrient stoichiometry within OBGC models potentially buffer the well-documented positive ocean carbon cycle feedback to future climate warming? A number of ESM's that have included representation of variable carbon to phosphorus stoichiometry within the ocean ecosystem component generally predict a more resilient response for future marine NPP and carbon export fluxes, with modest ~0 – <5% declines by year 2100 (Bopp et al., 2013; Cabré et al., 2015; Tanioka & Matsumoto; 2017; Kwiatkowski et al., 2018; Buchanan et al., 2018; Matsumoto et al., 2020; Kwon et al., 2022). Inclusion of variable phosphorus to carbon stoichiometry within the marine ecosystem component permits flexibility in phytoplankton phosphorus quotas. Such frugal use of nutrients allows phytoplankton to maintain similar growth rates under decreasing P flux as well as a shift towards increasing biomass C:P that partially compensates for warming induced changes to

ocean circulation and stratification. Galbraith and Martiny (2015) demonstrated with a simple box model that changes to the preformed phosphate concentration on the order of 100 nM within low latitude surface waters can produce up to 20 ppm shifts in atmospheric CO_2 concentrations, assuming P is the primary growth limiting nutrient. An OBGC modeling study incorporating representation of variable marine elemental stoichiometry found that adding this sensitivity buffered against a predicted decrease in global carbon export production on the order of ~3% for the 21st century (Tanioka & Matsumoto, 2017). Similarly, results from the recent inclusion of this process within the Pelagic Interactions Scheme for Carbon and Ecosystem Studies Quota (PISCES-QUOTA) model, suggest its effects on 21st century ocean carbon uptake are modest with up to a 3.5% underestimation as compared to fixed stoichiometry ESMs (Kwiatkowski et al., 2018). However, larger regional changes of up to 50% reductions or stimulations of marine NPP and carbon export were predicted which could have significant local to regional impacts on marine ecosystems and fisheries. The above studies have thus far considered adaptive nutrient quotas, while other phytoplankton adaptive strategies including altered physiological rates, trait-based evolution, and changes in grazing pressure could all potentially influence phytoplankton fitness and resilience with important controls on marine NPP and carbon export trends (Martiny et al., 2021).

As the next generation of OBGC models mature to better represent variable carbon to nutrient stoichiometry with the goal to study how this variability impacts the marine NPP and carbon export fluxes, an important missing element to this question is the role for changes in marine phytoplankton biodiversity to modulate the response. Most of the current generation of OBGC models represent the marine phytoplankton community with 1 – 3 PFTs, with the notable exception of the ECCO-Darwin OBGC model which simulates 35 up to 350 PFTs (e.g.,

Dutkiewicz et al., 2020; Juranek et al., 2020). This higher biodiversity model has been shown to more accurately represent the marine phytoplankton diversity regionally to globally, as gauged by such metrics as phytoplankton size distribution, biomass, size-fractionated NPP rates, and species richness. How does marine phytoplankton diversity and associated carbon to nutrient stoichiometric variability impact the regional to global patterns of carbon export? Based on current understanding, enhanced thermal stratification of the water column depresses the vertical nutrient input, favoring a shift to smaller sized pico-phytoplankton dominated by cyanobacteria possessing higher plasticity in cellular nutrient quotas. Thus, in a future warmer ocean with expanding stratification, the marine biodiversity response might be hypothesized to favor marine cyanobacteria such as *Prochlorococcus* and *Synechococcus* with elevated C:P cellular stoichiometry. While the shift to smaller phytoplankton may depress marine NPP rates, export of a portion of the resultant biomass with high C:P may partially buffer against reductions in marine carbon export and mitigate the expected positive feedback to warming by maintaining the strength of the ocean's biological carbon pump. In support of this hypothesis, observations from the Bermuda Atlantic Time-series station in the Sargasso Sea document a recent decline in marine NPP due to enhanced stratification, without a concomitant decline in carbon export, explained by a shift in the phytoplankton community composition in favor of cyanobacteria with higher cellular C:P stoichiometry (Lomas et al., 2022).

This paper describes the addition of three new pico-phytoplankton functional types, *Prochlorococcus*, *Synechococcus*, and pico-eukaryotes, to the OBGC component of the Community Earth System Model, with the goal to better characterize the role for marine phytoplankton biodiversity and associated variable cellular carbon to phosphorus stoichiometry in controlling marine carbon export patterns. The implementation builds from recent advances in

this OBGC model to incorporate variable C:P stoichiometry within all pertinent tracers of the marine ecosystem (Letscher et al., 2015; Wang et al., 2019) including phytoplankton, dissolved organic matter, and sinking particulate organic matter, to now include representation of six PFTs: *Prochlorococcus*, *Synechococcus*, pico-eukaryotes, nano-phytoplankton (including implicit coccolithophores), diatoms, and diazotrophs.

2. Model and Validation Data

The model is the Biogeochemical Elemental Cycling (BEC) model, which is the biogeochemistry and ecosystem component operating within the ocean circulation model (POP2) of the Community Earth System Model (CESM) v.1.2.2 (http://www.cesm.ucar.edu/models/cesm1.2/). The model resolution employed here is nominally 3º x 3º horizontally with 60 vertical layers (gx3v7 grid) that increase in thickness with depth in the water column. The ocean circulation is the output of the Parallel Ocean Program 2 (POP2) ocean circulation model using the final thirty-year forcing from years 1980 – 2009 of the CORE-II forcing (Smith et al., 2010) and includes parameter value changes to the isopycnal diffusivity (κ_{isop}) to partially account for the transport of unresolved equatorial jets (Getzlaff & Dietze, 2013).

The BEC tracks the cycling of key biogeochemical tracers (e.g., C, N, P, Fe, and O_2) amongst dissolved inorganic, dissolved organic, sinking particulate, and four plankton biomass pools (Moore et al., 2004). Net primary production in the model is partitioned amongst three PFTs–small phytoplankton (with implicit calcifiers), diatoms, and diazotrophs, which differ in their relative competitiveness for limiting nutrients (N, P, Si, and Fe). In addition to bottom-up nutrient and light control, phytoplankton mortality is controlled top-down by grazing from one zooplankton group. Version 1.2.2 of the BEC contains significant improvements to the cycling of

marine dissolved organic matter (Letscher et al., 2015). More recent model development for BEC v1.2.2 has incorporated variable phosphorus quotas for the three phytoplankton types (Wang et al., 2019) that depend on *in situ* simulated inorganic phosphate concentration following the linear relationship in Galbraith & Martiny (2015) but with an imposed minimum (110:1) and maximum (210:1) C:P value for all PFTs. This current work describes the addition of three new pico-phytoplankton groups with variable carbon to nutrient (P and Fe) stoichiometry to the BEC model, building from the code base for the variable 3 PFT phosphorus quota model of Wang et al., (2019). The 'small phytoplankton' group from the 3 PFT BEC model which jointly represented pico- and nano-sized phytoplankton has been reparameterized to more closely represent larger nano-phytoplankton. The newly named nano-phytoplankton along with the diatom and diazotroph groups are updated to represent variable C:P and C:Fe stoichiometry. The model retains one zooplankton group with Redfieldian stoichiometry. The marine ecosystem in the BEC model is thus represented by 6 phytoplankton and 1 zooplankton groups, or 6p1z.

Output of the pico-phytoplankton BEC model is validated for the simulation of chlorophyll a and NPP against the Sea-Viewing Wide Field-of-View Sensor (SeaWiFS) satellite mission climatology products (1997 – 2010) related to chlorophyll a concentration (NASA GSFC, 2018) and a model of carbon-based net primary productivity estimated from SeaWiFS data products (Behrenfeld et al., 2005; Westberry et al., 2008). Simulated nutrient concentrations from the pico-phytoplankton BEC model are compared against the World Ocean Atlas 2013 climatologies of nitrate, phosphate, and silicate (Garcia et al., 2013) and a global compilation of dissolved Fe concentrations (Tagliabue et al., 2012). Simulated pico-phytoplankton biomass are validated against the data assimilative niche modeling of Flombaum et al. (2013; 2020) that predicts field observed *Prochlorococcus*, *Synechococcus* from inputs of temperature and

irradiance (Flombaum et al., 2013) and pico-eukaryote biomass from inputs of temperature, irradiance, and dissolved nitrate (Flombaum et al., 2020). Simulated pico-phytoplankton C:P stoichiometry and biomass are compared against observations of populations from the North Atlantic, eastern Pacific, and eastern Indian Oceans of *Prochlorococcus*, *Synechococcus*, and pico-eukaryotes measured for C and P content (Baer et al., 2017; Lomas et al., 2021). Simulated total phytoplankton biomass C:P stoichiometry is compared against a global compilation of bulk particulate organic matter C, N, and P content (Martiny et al., 2014).

3. Methods

The addition of three pico-phytoplankton groups with variable carbon to nutrient stoichiometry introduces 12 additional tracers to the BEC model code: biomass carbon (C), chlorophyll (Chl), iron (Fe), and phosphorus (P) for each of the 3 pico-phytoplankton groups, termed 'Prochlorococcus' (pro), 'Synechococcus' (syn), and 'Pico-eukaryotes' (peuk). The 'small phytoplankton' group from BEC v1.2.2 and earlier versions has been renamed 'nano-phytoplankton' (nano) and retains the implicit calcifiers. Nano-phytoplankton as well as the diatoms (diat) and diazotroph (diaz) phytoplankton groups carry the same four biomass tracers (C, Chl, Fe, P) as the newly added pico-phytoplankton, with the addition of biomass silicon for diatoms. Variable biomass nitrogen (N) content is not considered at this time and phytoplankton biomass N:C is fixed for all six phytoplankton groups at a value of 0.1333 (C:N = 7.5) near the mean of open ocean suspended particles (Martiny et al., 2013b) and nutrient replete versus deplete cells across a range of phyla (Geider & La Roche, 2002).

Growth and mortality of each phytoplankton type is modeled with more than two dozen parameter values specific to each group including half saturation constants for nutrient uptake,

photosynthesis vs irradiance curves, Fe and P quotas, temperature thresholds for growth, contributions to detrital pools, and zooplankton grazing rates among others. Table 1 lists these parameter values for each phytoplankton group including the relevant literature sources. Where literature sources are lacking to inform the value for a particular parameter, the principle of allometric scaling is employed to assign values corresponding with cell size with the order of increasing cell size following: pro/syn/peuk < nano/diaz < diat.

Parameter	Description	Units	pro	syn	peuk	nano	diat	diaz	Reference
kFe	half sat. const. diss. iron	$mmol/m^3$	0.030e-3	0.040e-3	0.043e-3	0.055e-3	0.06e-3	0.04e-3	*Shire & Kustka, 2015; Timmermans et al., 2005; Hutchins et al., 2002*
kPO4	half sat. const. phosphate	$mmol/m^3$	0.008	0.01	0.015	0.04	0.07	0.025	*Lomas et al., 2014; Stukel et al., 2014; Garcia et al., 2015*
kDOP	half sat. const. diss. organic P	$mmol/m^3$	0.8	0.9	0.15	0.2	0.1	0.25	*Casey et al., 2009; Orchard et al., 2010; Sohm & Capone, 2006; Dyhrman & Ruttenberg, 200*
kNO3	half sat. const. nitrate	$mmol/m^3$	0.3	0.18	0.15	0.25	0.35	4.0	
kNH4	half sat. const. ammonium	$mmol/m^3$	0.005	0.008	0.011	0.02	0.035	0.4	
gQfe_0	initial Fe:C	ratio	80e-6	80e-6	90e-6	90e-6	90e-6	180e-6	*Boyd et al., 2015*
gQfe_min	minimum Fe:C	ratio	10.0e-6	10.0e-6	3.0e-6	3.0e-6	3.0e-6	6.0e-6	*Boyd et al., 2015*
FeOpt	threshold for reducing Fe quota	$mmol/m^3$	0.8e-3	0.8e-3	1.0e-3	1.6e-3	1.75e-3	1.5e-3	*Boyd et al., 2015*
gQp_0	initial P:C	ratio	1.042e-2	1.042e-2	1.111e-2	1.111e-2	1.111e-2	6.667e-3	*Galbraith & Martiny, 2015; Martiny et al., 2013*
gQp_min	minimum P:C	ratio	3.704e-3	5.208e-3	8.333e-3	8.333e-3	8.333e-3	3.333e-3	*Galbraith & Martiny, 2015; Martiny et al., 2013*
POpt	threshold for reducing P quota	$mmol/m^3$	0.5	0.5	0.75	1.0	1.0	0.5	*Galbraith & Martiny, 2015; Martiny et al., 2013*
	resulting max C:P	ratio	270	192	120	120	120	300	
	resulting max N:P	ratio	45	32	20	20	20	50	
alphaPI	initial slope of Photo-Irr curve	$mmolC\ m^2/mgChl\ W\ s$	1.00	1.09	0.7	0.83	0.88	0.2	*Stawiarski et al., 2017*
PCref	maximum C-spec. growth rate	d^{-1}	3.6	3.6	3.8	3.8	4.0	1.9	*Stawiarski et al., 2017*
thetaN_max	maximum Chl:N	ratio	3.33	2.20	3.55	3.00	4.00	2.00	*Stawiarski et al., 2017*
loss_thres	biomass where losses go to 0	$mmolC/m^3$	0.02	0.02	0.02	0.025	0.025	0.02	
temp_thres	temp. where Photo rates drop	ºC	13.0	4.0	-1.5	-10.0	-10.0	18.0	*Flombaum et al., 2013; 2020*
mort	mortality rate	d^{-1}	0.1	0.1	0.1	0.1	0.1	0.1	
agg_rate_max	maximum aggregation rate	d^{-1}	0.5	0.5	0.5	0.5	0.8	0.5	
agg_rate_min	minimum aggregation rate	d^{-1}	0.005	0.005	0.01	0.01	0.015	0.005	
z_umax_0	maximum zoopl. growth rate	d^{-1}	2.66	2.60	2.97	2.80	2.70	2.80	
z_grz	grazing coefficient	$mmolC/m^3$	1.3	1.6	1.95	1.8	1.58	1.3	
graze_zoo	routing of grazing to zoopl.	fraction	0.3	0.3	0.3	0.3	0.3	0.3	
graze_poc	routing of grazing to POC	fraction	0.07	0.09	0.13	0.28	0.40	0.03	*Lomas & Moran, 2011*
graze_doc	routing of grazing to DOC	fraction	0.06	0.06	0.06	0.06	0.06	0.06	*Letscher et al., 2015*
f_zoo_detr	fract. zoopl. losses to detrital	fraction	0.33	0.32	0.3	0.2	0.2	0.36	

Table 1. Description of phytoplankton parameters and values from the PICO simulation of the BEC model.

Phytoplankton iron uptake half saturation constants are prescribed with cyanobacteria having the lowest values (pro = 30 pM; syn+diaz = 40 pM), followed by pico-eukaryotes (43 pM), nano-eukaryotes (55 pM), and the large celled diatoms (60 pM) following the culture studies of Shire and Kustka, (2015) and Timmermans et al., (2005) and the field study of Hutchins et al., (2002) (Table 1). Phosphate half saturation constants are selected based on the

field study from the Sargasso Sea of Lomas et al., (2014), the culture study of Garcia et al., (2015), and the Amazon River plume ecosystem modeling work of Stukel et al., (2014) with kPO4 values increasing from a value of 8 nM for pro, 10 nM for syn, 15 nM for peuk, 25 nM for diaz, 40 nM for nano, and 70 nM for diatoms. Semilabile dissolved organic phosphorus (DOP) is bioavailable for phytoplankton to utilize as a P source when phosphate levels are low in the BEC model (Letscher et al., 2015) with the half saturation constants for its uptake selected based on several field studies from the Sargasso Sea and eastern North Pacific (Dyhrman & Ruttenberg, 2006; Sohm & Capone, 2006; Casey et al., 2009; Orchard et al., 2010). Following these studies, eukaryotes and diazotrophs are assigned the lowest half saturation values for DOP uptake ranging from 100 – 250 nM, with higher kDOP values ranging from 800 – 900 nM for the two cyanobacteria groups. Half saturation constants for ammonium are assigned following allometric scaling in the range 5 – 35 nM. Nitrate uptake half saturation constants are similarly assigned following allometric scaling in the range 150 – 350 nM, with exceptions for syn and peuk which are assigned the lowest values of 180 and 150 nM respectively, owing to their demonstrated increased affinity for nitrate relative to pro in the Sargasso Sea (e.g., Glover et al., 1988; Fawcett et al., 2013) and observed correlations between peuk abundance and *in situ* nitrate (Flombaum et al., 2020). Diazotroph kNH4 and kNO3 are set to the highest value across the 6 PFTs to reflect its reliance on internally fixed N for a significant but not exclusive fraction of its N quota (Knapp, 2012).

Phytoplankton iron quotas in the BEC model allow for flexibility in phytoplankton biomass Fe:C based on *in situ* dissolved iron concentrations, varying in the range of 3 μmol:mol to 180 μmol:mol (Table 1). Following the field study of Boyd et al., (2015), eukaryotes are assigned the lowest minimum iron quotas followed by diazotrophs and non-N-fixing

292 cyanobacteria (*Prochlorococcus* and *Synechococcus*). The diazotroph group is assigned the
293 highest maximum iron quotas based on the high iron requirement of the nitrogen-fixing enzyme
294 nitrogenase (Berman-Frank et al., 2007). Phytoplankton iron quotas are reduced linearly when *in*
295 *situ* dissolved Fe concentrations fall below a prescribed threshold (FeOpt), set to 1.75 nM for
296 diatoms, 1.6 nM for nano, 1.5 nM for diaz, 1.0 nM for peuk, and 0.8 nM for pro and syn
297 (Wisemann et al., under review).

298 Variable phosphorus quotas are implemented here for the six phytoplankton group BEC
299 model following the approach introduced in Wang et al. (2019) and similar to the variable Fe:C
300 approach described above. Variable phytoplankton biomass P:C is modeled as a function of *in*
301 *situ* dissolved phosphate concentration using the linear relation detailed in Galbraith & Martiny
302 (2015) diagnosed from a global compilation of suspended particulate organic phosphorus and
303 carbon concentrations. Each PFT P:C quota (gQp) is computed from:

304 $$gQp = \left[\left(\frac{gQp\_0 - gQp\_min}{POpt}\right) \times PO4\right] + gQp\_min \qquad \text{PO4} < \text{POpt} \qquad \text{(Eq. 1)}$$

305 $$gQp = gQp\_0 \qquad \text{PO4} \geq \text{POpt}$$

306 where PO4 is the *in situ* dissolved inorganic phosphate concentration (μM) and gQp_0 and
307 gQp_min describe the minimum and maximum P:C quota (see Table 1). Equation 1 linearly
308 decreases the phytoplankton P:C quota (increases its C:P ratio) below a prescribed threshold
309 (POpt; range 0.5 – 1.0 μM across PFTs), from its initial maximum value, currently prescribed at
310 gQp_0 = 0.01111; C:P = 90:1 for the eukaryotes (peuk+nano+diat), gQp_0 = 0.01042; C:P =
311 96:1 for the cyanobacteria, and gQp_0 = 0.006667; C:P = 150:1 for diazotrophs, towards a
312 minimum P:C quota that varies for each PFT (Table 1). This formulation is similar in approach
313 to that presented in Galbraith & Martiny (2015). Here, field observations of surface ocean
314 particulate organic carbon and phosphorus (of which autotrophic biomass is a significant

contributor) were found to fit a linear function of *in situ* phosphate concentration. The formulation presented here prescribes differing P:C versus PO4 slopes and y-intercepts for each PFT set by the choice of gQp_min. Field-based estimates of cell-sorted biomass C:P and N:P for *Prochlorococcus*, *Synechococcus*, and pico-eukaryotes from the Sargasso Sea (Martiny et al., 2013a) and elsewhere (Baer et al., 2017; Lomas et al., 2021) are used to assign values of gQp_min with a maximum C:P of 300:1 for diazotrophs, a C:P of 270:1 for *Prochlorococcus* and 192:1 for *Synechococcus*, and a maximum C:P of 120:1 for peuk, nano, and diat (retained from the variable C:P BEC model; Wang et al., 2019).

Based on the phytoplankton niche modeling of Flombaum et al. (2013; 2020), each phytoplankton group in the BEC is assigned a temperature threshold below which photosynthesis rates and thus growth rates are depressed, with *Prochlorococcus* and diazotroph niches favoring warmer temperatures above 13ºC and 18ºC, respectively. *Synechococcus* and pico-eukaryote growth decreases as temperatures fall below 4ºC and -1.5ºC, respectively, while nano-phytoplankton and diatom growth rates are not depressed as a function of temperature (temp_thres value set to -10ºC in Table 1).

Physiological response to light parameters describing the pico-phytoplankton are assigned based on the culture study of Stawiarski et al. (2017) in which two strains of *Prochlorococcus* (HL RCC 296, LL RCC 162), one *Synechococcus* strain (RCC 30), and four pico-eukaryote species *Triparma eleuthera* (RCC 212), *Micromonas pusilla* (RCC 1677), *Picochlorum* sp. (TCC 289), and *Nannochloropsis granulata* (RCC 438) from the Roscoff culture collection (Vaulot et al., 2004) were studied. Following this study, cyanobacteria are assigned slower maximum growth rates compared with eukaryotes, in the range 1.9 – 4 d^{-1} (based on a 24-hour light period). Stawiarski et al. (2017) found that light affinity is inversely related to

the maximum growth rate. *Prochlorococcus* and *Synechococcus* are assigned the highest light affinities, as encoded within the 'alphaPI' model parameter which describes the initial slope of the photosynthesis-irradiance curve, with decreasing affinities for the faster growing eukaryotes (Table 1). The maximum Chl:N, the 'thetaN_max' model parameter, is assigned inversely proportional to maximum growth rate with the exception of *Synechococcus* which exhibits lower Chl:C in line with the results of Stawiarski et al. (2017).

Grazing on each of the six phytoplankton groups in the updated BEC model is carried out by one adaptive zooplankton group. Grazing rates are largely unconstrained by field data. In the BEC model, maximum grazing rates, 'z_umax_0' parameter, are adjusted to achieve satisfactory biomass distributions and C:P stoichiometry for each phytoplankton group as validated against phytoplankton niche modeling and flow-sorted biomass stoichiometry distributions. Variable fractions of phytoplankton biomass are routed to zooplankton losses to detritus (e.g., fecal pellets) and particulate organic matter pools resulting from zooplankton grazing (Table 1). Each PFT's contribution to the sinking export flux following grazing varies from a minimum of 3% for diazotrophs to a maximum of 40% for diatoms ('graze_poc'; Table 1) informed in part by pigment biomarker analyses of the sediment trap flux in the Sargasso Sea (Lomas & Moran, 2011). Zooplankton contribute varying proportions of grazed phytoplankton biomass to detritus (POC) based on the PFT grazed, ranging from a minimum of 20% for nano-phytoplankton and diatoms to a maximum of 36% when grazing diazotrophs ('f_zoo_detr'; Table 1). Grazing of phytoplankton biomass also contributes 6% to the dissolved organic matter pool following the inverse model diagnosed rate from our previous work (Letscher et al., 2015). In the BEC model, combinations of two or more phytoplankton types can be grouped together in 'grazee' classes, for which zooplankton grazing rates are computed jointly based on the total amount of biomass

in each simulated *in situ* 'grazee' class. Experimentation was carried out to decide which combinations of phytoplankton groups in each 'grazee' class achieved distributions of phytoplankton biomass, NPP, and dissolved nutrients that best matched observations. A model configuration in which all six PFTs were ungrouped, i.e., parameter grazee_ind was set equal to auto_ind, the unique index of each of the six PFTs, was chosen.

BEC simulations were carried out for sixty model years from initial conditions, allowing the upper ocean ecosystem to achieve tracer equilibrium. After selection of the set of parameter values that best matched observational constraints, a longer 300 model year simulation was performed, repeating the 30-year (1980 – 2009) CORE-II forcing for a total of ten repetitions. The annually averaged output from the final twenty years of this simulation were averaged and is presented in all results to follow. Reported flux variability represents ±1 S.D. of the mean from the twenty years of output. The BEC simulation containing the additional pico-phytoplankton groups for a total of 6 PFTs is termed PICO. In Section 4, this simulation is compared against two similarly forced previous versions of the BEC model: a variable C:P stoichiometry version with 3 PFTs herein termed VAR-3 (Wang et al., 2019) and a 3 PFT version with Redfield stoichiometry governing phytoplankton dynamics herein termed RED-3 (Letscher et al., 2015).

4. Results

Chlorophyll a & NPP– Sea surface chlorophyll a (chl a) concentrations [mg m^{-3}] from the PICO simulation and the SeaWiFS satellite climatology are shown in Figure 1a-b. BEC simulated chl a captures the overall pattern of lowest concentrations within the subtropical ocean gyres, highest concentrations within coastal and subpolar zones, and intermediate concentrations in upwelling regions and subtropical to mid-latitude transitions zones (Fig. 1). The PICO

simulation exhibits an overall global negative mean bias in chl a (–6%; Table 2) relative to the SeaWiFS climatology, reducing by a factor of ~3 compared with the 3 PFT variable C:P stoichiometry BEC model (VAR-3) and an earlier version containing 3 PFTs and Redfield stoichiometry (RED-3) (Table 2).

	PICO		VAR-3		RED-3	
	r-correlation	**mean bias**	**r-correlation**	**mean bias**	**r-correlation**	**mean bias**
Chl a	0.087	-6%	0.218	-19%	0.167	-17%
CbPM NPP	0.241	+3%	0.108	+0.5%	0.153	-3.0%
$[NO_3^-]$	0.938	0.01 µM	0.940	0.01 µM	0.920	0.01 µM
$[PO_4^{3-}]$	0.940	0.02 µM	0.932	-0.01 µM	0.944	0.03 µM
$[SiO_4^{4-}]$	0.935	0.01 µM	0.936	1.14 µM	0.932	-0.01 µM
[dFe]	0.398	0.18 nM	0.332	-0.14 nM	0.374	0.04 nM

Table 2. Comparison metrics for PICO, VAR-3, and RED-3 simulated chlorophyll a and NPP versus satellite (SeaWiFS) climatology estimates using the CbPM model. Metrics for dissolved nutrients from the same three simulations are compared versus the World Ocean Atlas 2013 (NO_3^-, PO_4^{3-}, SiO_4^{4-}) and Tagliabue et al. (2012) Fe data compilation.

Vertically integrated annual net primary productivity (NPP) [g C m^{-2} yr^{-1}] from the PICO simulation is provided along with the Carbon-based Productivity Model estimate of NPP from the SeaWiFS climatology (Westberry et al., 2008) (Figure 1c-d). The globally integrated annual NPP from PICO is 51.4 ± 0.75 Pg C yr^{-1}, within the range of satellite-based estimates – 60-67 Pg C yr^{-1} (Behrenfeld et al., 2005), 52 Pg C yr^{-1} (Westberry et al., 2008; Silsbe et al., 2016), 58 ± 7 Pg C yr^{-1} (Buitenhuis et al., 2013). Highest rates of annual NPP are simulated in the equatorial Pacific, Arabian Sea, and the South Pacific and North Atlantic eastern boundary upwelling zones, reaching rates of ~400 – 600 g C m^{-2} yr^{-1} in the PICO simulation, which is approximately

403 25 – 75% greater than those estimated by the CbPM. The lowest rates of NPP simulated by PICO
404 are found within the Arctic Ocean, which are approximately one-quarter of those estimated by
405 CbPM. The PICO simulation also simulates higher rates of NPP as compared to CbPM within
406 the mid-latitudes of both hemispheres, especially near the western boundary of each ocean basin.
407 Overall, the PICO simulation exhibits a small positive mean bias of +3% in estimated global
408 annual NPP rates when comparing binned 3ºx3º pixels with the CbPM SeaWiFS climatology
409 (Table 2).
410

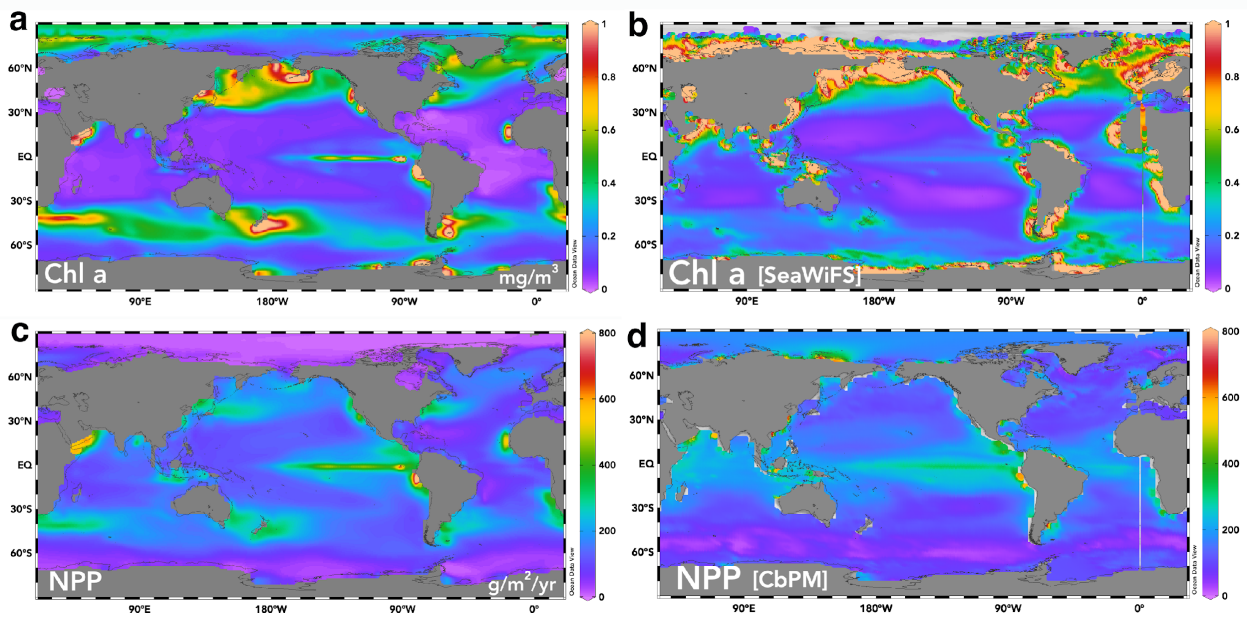

411

412 **Figure 1.** PICO simulated 20-yr averaged sea surface chlorophyll a [mg m^{-3}] (a), climatological
413 average sea surface chlorophyll a from the SeaWiFS satellite during 1997-2010 (b), PICO
414 simulated 20-yr averaged NPP [g C m^{-2} yr^{-1}] (c), and from the CbPM model using SeaWiFS
415 satellite data from the same era (d) (Westberry et al., 2008).
416

417 *PFT contributions to spatial NPP patterns* – The fractional contribution of each of the six
418 PFTs to simulated NPP rates within the PICO simulation is shown in Figure 2. The majority of

NPP within the five subtropical gyre regions is contributed by *Prochlorococcus* (fraction of NPP ~ 0.50 – 0.90), with a general western intensification (Fig. 2a). *Synechococcus* NPP is similarly elevated within the subtropics, albeit at lower fractional contributions in the range ~0.06 – 0.12 (Fig. 2b). *Prochlorococcus* and *Synechococcus* are mostly absent from the polar oceans due to their imposed temperature threshold of 13ºC and 4ºC for positive growth rates (Flombaum et al., 2013; Table 1). Pico-eukaryotes dominate NPP (fraction of NPP > 0.80) in many of the eastern boundary and mid-latitude regions of the world ocean in PICO (Fig. 2c). Elsewhere, pico-eukaryote contribution to simulated NPP is much reduced, in the range ~0.02 – 0.10. Nano-phytoplankton contribute variably to NPP rates within a range of 0.02 – 0.20 throughout the world ocean in PICO (Fig. 2d). Lowest simulated contributions are found in the eastern and equatorial upwelling regions; highest contributions are located in the polar oceans. Diatoms dominate simulated NPP rates (fraction > 0.80) within the subpolar and polar oceans as well as the equatorial Pacific (Fig. 2e), with lowest fractional contributions to NPP (~0.01 – 0.05) located within the subtropical gyres. Diazotrophs contribute < 0.07 to simulated NPP rates and are absent from the subpolar and polar oceans, due to the imposed minimum temperature of 18ºC for positive growth rates (Table 1). Highest diazotroph contributions to NPP rates are found within the western tropical to subtropical North and South Pacific Oceans (~0.04 – 0.07) (Fig. 2f), similar to other OBGC model simulations that incorporate variable nutrient stoichiometry (e.g., Wang et al., 2019).

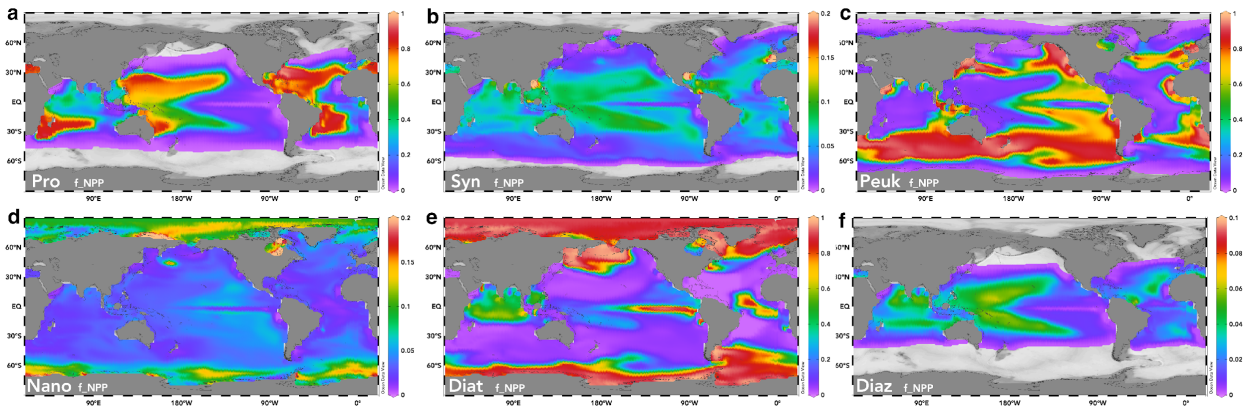

Figure 2. Fraction of vertically integrated, annual marine NPP attributable to each PFT from the PICO simulation. (a) *Prochlorococcus*, (b) *Synechococcus*, (c) pico-eukaryotes, (d) nano-phytoplankton, (e) diatoms, (f) diazotrophs. Note change in range in panels a,c,e from panels b,d, and panel f.

Nutrients – Upper ocean (0 – 500 m) simulated dissolved nutrient concentrations from PICO have been compared against the World Ocean Atlas (WOA) 2013 climatology (Garcia et al., 2013) for nitrate (NO_3^-), phosphate (PO_4^{3-}), and silicate (SiO_4^{4-}) and a global compilation of dissolved Fe (dFe) measurements (Tagliabue et al., 2012). Table 2 provides the r-correlation parameter and mean bias (µM) from a regression of log-transformed model-observation pairs. Dissolved NO_3^-, PO_4^{3-}, and SiO_4^{4-} are equally well correlated with WOA nutrients, exhibiting r-correlation coefficients of ~0.94 and mean biases of +0.01 µM NO_3^-, +0.02 µM PO_4^{3-}, and +0.01 µM SiO_4^{4-}. PICO simulated dFe is the most weakly correlated nutrient with observational data, r = 0.40, with a mean bias of +0.18 nM. The PICO upper ocean dissolved nutrient mean biases are similar to those of the other variable C:P stoichiometry simulation, VAR-3, and the Redfield simulation, RED-3, with a notable improvement to the mean bias of SiO_4^{4-} from VAR-3 (Table 2).

457 *Biomass* – PICO simulated biomass (µg C L^{-1}) is compared against the data assimilative
458 niche model output for *Prochlorococcus* and *Synechococcus* (Flombaum et al., 2013) and pico-
459 eukaryotes (Flombaum et al., 2020) binned by 3ºx3º pixels. Simulated pico-phytoplankton
460 biomass correlation coefficients with the niche model output range from 0.485 (pico-eukaryotes)
461 to 0.637 (*Prochlorococcus*) (Table 3). However, significant negative biases are present within
462 PICO simulated *Prochlorococcus* biomass (–56%), *Synechococcus* biomass (–85%), and pico-
463 eukaryotes biomass (–76%) (Table 3). PICO pico-phytoplankton biomass has also been
464 compared against a globally compiled field-based dataset of flow-sorted populations (Baer et al.,
465 2017; Lomas et al., 2021), yielding metrics of: *Prochlorococcus* biomass (+76%, r = 0.199),
466 *Synechococcus* biomass (–72%, r = 0.245), and pico-eukaryotes biomass (–72%, r = 0.142)
467 (Table 3).
468

	r-correlation	mean bias	n
Pro C niche	0.637	-56%	24,447
Syn C niche	0.459	-85%	33,101
Peuk C niche	0.485	-76%	39,244
Pro C:P	0.120	-5.6%	55
Syn C:P	0.229	-17.1%	44
Peuk C:P	0.021	+11.1%	50
POC:POP	0.245	+20%	4651
Pro C	0.199	+76%	2188
Syn C	0.245	-72%	4120
Peuk C	0.142	-72%	4158

469

470 **Table 3.** Comparison metrics for PICO simulated pico-phytoplankton biomass versus the data
471 assimilative niche models of Flombaum et al. (2013; 2020) (Pro C niche, Syn C niche, Peuk C
472 niche); versus pico-phytoplankton biomass C:P stoichiometry (Baer et al., 2017; Lomas et al.,
473 2021) (Pro C:P, Syn C:P, Peuk C:P) and biomass C (Pro C, Syn C, Peuk C); and versus bulk
474 particulate organic matter C:P stoichiometry (Martiny et al., 2014) (POC:POP).

475

476 *Phytoplankton Stoichiometry* – Euphotic zone-averaged PFT C:P stoichiometry from the
477 PICO simulation is shown in Figure 3. *Prochlorococcus* (Fig. 3a) and diazotrophs (Fig. 3f)
478 exhibit the greatest range in cellular C:P stoichiometry, with the minimum stoichiometry found
479 within the eastern equatorial Pacific Ocean, C:P = ~90 for pro; C:P = ~150 for diaz, increasing to
480 maximum cellular C:P = ~250 – 300 within the North and South Atlantic subtropical gyres.
481 Elevated C:P stoichiometry for *Prochlorococcus* and diazotrophs is also found within the other
482 three subtropical gyre regions, with typical values in the range ~180 – 300. *Synechococcus* (Fig.
483 3b), pico-eukaryotes (Fig. 3c), nano-phytoplankton (Fig. 3d), and diatoms (Fig. 3e) all exhibit
484 similar geographical variability in cellular C:P stoichiometry to *Prochlorococcus* and
485 diazotrophs, with elevated values typical of the five subtropical ocean gyre regions, syn C:P =
486 ~150 – 210; peuk + nano + diat C:P = ~110 – 125. Phytoplankton C:P stoichiometry is ~25 –
487 80% more elevated within the western half of each subtropical gyre relative to the eastern half.

488

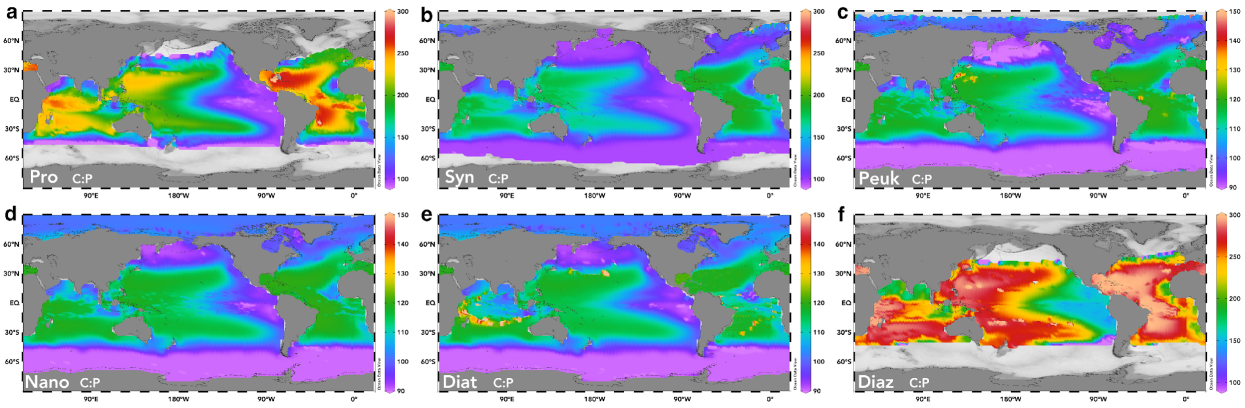

489

490 **Figure 3.** Euphotic zone averaged cellular C:P stoichiometry for each PFT from the PICO
491 simulation. (a) *Prochlorococcus*, (b) *Synechococcus*, (c) pico-eukaryotes, (d) nano-
492 phytoplankton, (e) diatoms, (f) diazotrophs.

493

494 PICO simulated *Prochlorococcus*, *Synechococcus*, and pico-eukaryotes cellular C:P
495 stoichiometry has been compared against a subset of the cell-sorted population dataset for which
496 biomass P was measured (Baer et al., 2017; Lomas et al., 2021). PICO simulated
497 *Prochlorococcus* C:P exhibits the smallest mean bias of –6% below the average field-based
498 estimate of C:P = 221 (Table 3). PICO simulated *Synechococcus* C:P has a negative mean bias of
499 –17% below the field estimate of 187. PICO simulated pico-eukaryotes exhibited a positive
500 mean bias compared to field estimates at +11% above the field estimate of 103. PICO simulated
501 total autotrophic biomass C:P stoichiometry is compared with a global compilation of surface
502 ocean suspended organic matter C:P stoichiometry (Martiny et al., 2014), exhibiting a positive
503 mean bias of +20% above the field-based estimate of POC : POP = 171 : 1 (Table 3).
504 *Sinking carbon export* – The sinking particulate organic carbon flux through the 100
505 meter depth horizon ($POC_{exp,100m}$) from the PICO simulation is plotted in Figure 4a. $POC_{exp,100m}$
506 exhibits a similar geographical distribution as simulated NPP (Fig. 1c), with maximum rates of
507 ~90 – 120 g C m^{-2} yr^{-1} found within the eastern equatorial Pacific, Peruvian, and Arabian Sea
508 upwelling regions as well as the SW Atlantic Ocean and minimum rates, < 20 g C m^{-2} yr^{-1},
509 within the five subtropical ocean gyres and their bordering tropical regions, the Southern Ocean,
510 and the Arctic Ocean. Other regions exhibiting elevated $POC_{exp,100m}$ include the eastern boundary
511 upwelling zones and the subtropical to mid-latitude transition zones with rates in the range ~40 –
512 70 g C m^{-2} yr^{-1}. The pico-phytoplankton contribution to $POC_{exp,100m}$ is greatest across the tropics,
513 subtropics, and mid-latitudes (Fig. 4b), with a fractional contribution in the range ~0.50 – 0.70.
514 In both hemispheres, pico-phytoplankton make their largest contribution to sinking POC export
515 in the mid-latitudes (~40 – 50 ºN and ºS), approaching 65 – 70% of $POC_{exp,100m}$., with minima

516 (~0.10 – 0.30) estimated for the subpolar, polar, and equatorial Pacific Oceans. The globally
517 integrated $POC_{exp,100m}$ flux below 100 m from PICO is 7.0 ± 0.1 Pg C yr^{-1}; within the range of
518 observational-, satellite-, and model-based estimates of global marine export production, e.g., 4 –
519 14 Pg C yr^{-1} (summarized in Emerson, 2014; Britten & Primeau, 2016; Siegel et al., 2014;
520 Henson et al., 2011). It should be noted when comparing the PICO carbon export flux to other
521 estimates from the literature that DOC export below 100 m contributes an additional ~2.1 Pg C
522 yr^{-1} of carbon export production in the BEC model (Letscher et al., 2015; Letscher & Moore,
523 2015) bringing estimated total organic carbon export below 100 m to ~9.1 Pg C yr^{-1}.
524

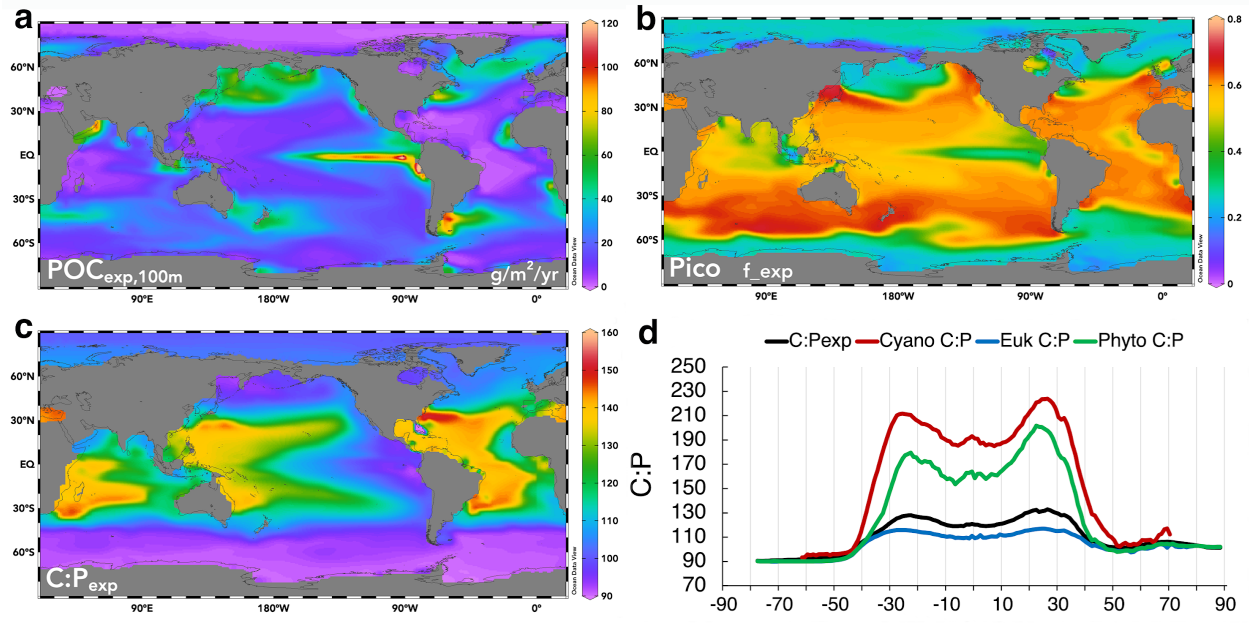

525

526 **Figure 4.** PICO simulated 20-yr averaged sinking particulate organic carbon export below 100 m
527 $POC_{exp,100m}$ [g C m^{-2} yr^{-1}] (a), the fraction of total $POC_{exp,100m}$ attributable to pico-phytoplankton
528 (pro + syn + peuk) (b), the C:P stoichiometry of sinking organic particles $C:P_{exp}$ at 100 m (c),
529 and the zonal mean $C:P_{exp}$ at 100 m (black line), C:P of cyanobacteria (pro + syn + diaz; red
530 line), C:P of eukaryotic phytoplankton biomass (peuk + nano + diat; blue line), and C:P of total
531 phytoplankton (green line) within the upper 100 m (d).

The C:P stoichiometry of the sinking organic particulate flux at 100 m ($C:P_{exp}$) from the PICO simulation is shown in Fig. 4c. Carbon rich/P-poor stoichiometry for $C:P_{exp}$ is found in the ocean tropics and subtropics, being a function of both the large contribution of pico-phytoplankton productivity (Fig. 2) in these regions as well as the elevated C:P stoichiometry of the cyanobacteria (pro + syn + diaz) PFTs inhabiting these regions (Fig. 4d). Sinking particulate export C:P stoichiometry exhibits global maxima within the western subtropical gyres of each basin, reaching values of ~140 – 150 (Fig. 4c). C:P export stoichiometry is elevated elsewhere within the subtropics, ~120 – 140, near Redfieldian in the mid-latitudes and the Arctic Ocean, and depressed within the eastern equatorial Pacific, subpolar North Pacific, and the Southern Ocean, exhibiting values in the range ~90 – 105. The zonal mean $C:P_{exp}$ is near the minimum imposed value of 90 for eukaryotic phytoplankton groups south of 50 ºS and near ~100 north of 50 ºN where the phytoplankton community is dominated by diatoms and other eukaryote groups (Fig. 2). Maximal zonal mean $C:P_{exp}$ is found at subtropical latitudes exhibiting values of ~128 at 23 ºS and a slightly higher value of ~133 at 26 ºN in the northern hemisphere (Fig. 4d). Cyanobacteria phytoplankton (pro + syn + diaz), eukaryotic phytoplankton (peuk + nano + diat), and the total phytoplankton community C:P stoichiometry all exhibit similar latitudinal patterns with high latitude minima and subtropical maxima (Fig. 4d). Cyanobacteria phytoplankton C:P varies between ~96 – 223, eukaryotic phytoplankton C:P varies between ~90 – 117, with total phytoplankton C:P varying between ~90 – 202.

5. Discussion

554 Pico-phytoplankton were found to make their largest contribution to marine NPP within
555 the tropical and subtropical ocean, reaching contributions of ~50 – 90% within the latitudinal
556 range 45ºN – 45ºS (Fig. 2). In general, *Prochlorococcus* dominates NPP within the subtropical
557 gyre regions, transitioning to dominance by pico-eukaryotes both equatorward and poleward of
558 ~30º latitude to ~45º. *Synechococcus* follows a similar spatial pattern as *Prochlorococcus* but
559 never dominates the phytoplankton community, with fractional contributions peaking at ~10 –
560 12% in the subtropical gyres. Diazotrophs, which are parameterized to represent the
561 cyanobacteria lineages of *Trichodesmium* and *Crocosphaera* in the BEC model, make a smaller
562 yet important additional contribution in these same low-latitude regions. The pico-phytoplankton
563 and diazotroph groups within the PICO simulation were assigned the largest cellular C:P
564 plasticity and higher minimum temperature thresholds for growth (Table 1) than the larger nano-
565 phytoplankton and diatoms, with the pico-phytoplankton niche being realized within the nutrient-
566 poor, high temperature waters of the low latitudes. The three pico-phytoplankton PFTs in PICO
567 contributed to globally integrated NPP at a percentage of 16.6 ± 0.4% for *Prochlorococcus*, 3.9 ±
568 0.5% for *Synechococcus*, and 37.1 ± 0.6% for pico-eukaryotes, for a total pico-phytoplankton
569 contribution of 57.6 ± 0.8% to marine NPP (Table 4). These estimates for global NPP
570 attributable to *Prochlorococcus* and *Synechococcus* within PICO are approximately double and
571 one-quarter, respectively, compared to an independent estimate based on data assimilative
572 modeling of niche partitioning, (pro = 8.5%, syn = 16.7%, Flombaum et al., 2013), however both
573 model estimates converge on a combined pro + syn contribution to marine NPP of ~20 – 25%.
574 Nano-phytoplankton contribute 3.6 ± 0.7% of global NPP in PICO (likely an underestimate, e.g.,
575 Brewin et al., 2010; Juranek et al., 2020), concentrated in the Southern Ocean, the subpolar and
576 Arctic Ocean, as well as the eastern tropical Pacific Ocean (Fig. 2d). Diatoms are the largest

577 contributor to global marine NPP in PICO, contributing 37.5 ± 0.5%, concentrated in the
578 subpolar and polar oceans as well as the equatorial Pacific upwelling (Table 4; Figure 2d). This
579 rate of diatom contribution to global NPP is consistent with the ~38-43% contribution estimated
580 from marine biogenic silica budgets (Nelson et al., 1995). Diazotrophs contribute 1.2 ± 0.04% to
581 marine NPP in PICO (Table 4), concentrated in the same tropical and subtropical regions as
582 pico-phytoplankton, especially the western tropical and subtropical Pacific Ocean (Fig. 2e).
583

PFT	**% of NPP**	**% of POCexp**
Procholorcoccus	16.6	14.9
Synechococcus	3.9	12.6
Pico-eukaryotes	37.1	18.1
Nano-phytoplankton	3.6	9.9
Diatoms	37.5	31.2
Diazotrophs	1.2	13.4
Σ Pico-phytoplankton	57.6	45.6

584

585 **Table 4.** Percentages of globally integrated marine NPP and $POC_{exp,100m}$ attributable to each
586 PFT.
587

588 Ecosystem processing of the newly fixed organic matter by each phytoplankton PFT
589 contributes to the detrital particulate organic matter pools, which constitute the source terms to
590 the sinking export fluxes of POC_{exp} and particulate organic phosphorus (POP_{exp}) in the BEC
591 model. These processes include losses to the detrital pool upon grazing by zooplankton,
592 zooplankton contributions to the detrital pool as a result of grazing (e.g., fecal pellet production),
593 and aggregation and sinking of phytoplankton biomass upon cell mortality within the BEC
594 model (Moore et al., 2004). The parameter values governing these processes were prescribed in a
595 size-scaling manner across the six PFTs in PICO (Table 1), with the pico-phytoplankton

596 contributing the smallest to the particulate sinking fluxes, increasing with diazotrophs and nano-
597 plankton, to the largest contribution from diatoms. The fractions of pico-phytoplankton grazing
598 and zooplankton losses that accumulate within the particulate fluxes were prescribed in the range
599 0.07 – 0.33 (Table 1), at the upper end of estimates based on pigment biomarker analyses of the
600 sediment trap flux collected from the Sargasso Sea (Lomas & Moran, 2011). The higher
601 estimates for pico-phytoplankton detrital contributions were needed to export enough N and P
602 below the euphotic zone to prevent spurious accumulation of NO_3^- and PO_4^{3-} concentrations in
603 the upper layers of the subtropics. The nano-phytoplankton and diatom contributions to NPP are
604 <5% each over much of the subtropical regions in PICO (Fig. 2), which are biased low compared
605 to field observations (e.g., Nelson & Brzezinski, 1997; Brzezinski et al., 2011; Juranek et al.,
606 2020) and may potentially explain the low N and P export efficiency, partially satisfied by
607 prescribed elevated pico-phytoplankton detrital contributions in PICO. PFT-specific parameters
608 linked to the detrital contributions are held constant in PICO, however future formulations of the
609 BEC model could include parameterizations that are dependent on *in situ* temperature, PFT
610 growth rate, grazing rate, or nutrient limitation status among others.

611 Within PICO, pico-phytoplankton contribute nearly half (45.6 ± 0.3%) of the globally
612 integrated $POC_{exp,100m}$ flux through 100 meters when accounting for both direct (e.g.,
613 aggregation) and indirect (e.g., zooplankton processing of pico-produced organic matter)
614 contributions. Approximately 40% of the pico-phytoplankton total is contributed by pico-
615 eukaryotes (18.1 ± 0.2%), an additional third contributed by *Prochlorococcus* (14.9 ± 0.1%), and
616 a quarter contributed by *Synechococcus* (12.6 ± 0.1%) (Table 4). Pico-phytoplankton dominate
617 the phytoplankton contribution to carbon export across large areas of the tropics, subtropics, and
618 mid-latitudes (Fig. 4b), which is an emergent result from the added phytoplankton biodiversity,

representation of variable carbon to phosphorus cellular stoichiometry, and ecosystem processing of the detrital pool mediated by zooplankton grazing. Perhaps counterintuitively, pico-phytoplankton contribution to carbon export peaks in importance (~0.65 – 0.7), not where their greatest environmental niche is realized, i.e., the high light, low nutrient waters of the oligotrophic subtropical gyres, but at mid-latitudes, ~35 – 45º, driven largely by regional maxima in C:P stoichiometry (Fig. 4c).

The estimate of pico-phytoplankton contribution to sinking carbon export in PICO (~46%) is approximately 80% their combined contributions to global NPP (~58%), in partial agreement with inversions of PFT-specific observational data from the equatorial Pacific and Arabian Sea suggesting that pico-phytoplankton contribute to carbon export at rates comparable to their contribution to NPP (Richardson & Jackson, 2007). Group specific C export fraction to NPP fraction ratios, computed from Table 4, range from a minimum of ~0.5 to ~3.2, within the range of the available group-specific estimates diagnosed from a range of field data, ~0.1 to ~4.5 (Richardson & Jackson, 2011; Stukel & Landry, 2010; Lomas & Moran, 2011; Fawcett et al., 2011; Stukel et al., 2013), albeit at the higher end especially for Pro and Syn which are 0.9 and 3.2 in PICO and ~0.1 and ~0.1 to ~0.4 from the literature (Lomas & Moran, 2011; Fawcett et al., 2011; Stukel et al., 2013), respectively. A notable outlier is the C export fraction to NPP fraction ratio for diaz which is ~11 in PICO. Dissolved organic matter (DOM) contributes ~20-25% of total organic carbon export production in the CESM (Letscher et al., 2015). We are unable to provide an estimate of each PFT contribution to the DOM export flux, as DOM export is spatially and temporally offset from its region of production, and the model does not track DOM sourced from individual PFTs. Each PFT contributes a constant fraction of its newly produced

641 organic matter to the DOM pool; therefore, PFT contributions to DOM export should generally
642 track the proportions of PFT contributions to NPP (e.g., Table 4).

643 The regions located immediately along the poleward and western edges of the surface
644 western boundary currents of the subtropical gyre regions of each ocean basin exhibit elevated
645 $POC_{exp,100m}$ fluxes on the order of ~50 – 90 g C m^{-2} yr^{-1} (Fig. 4a), approximately ~2-3 fold higher
646 as compared to the adjacent regions. These so-called 'gyre recirculation regions' of the surface
647 western boundary currents are characterized by strong eddying flow and enhanced lateral
648 nutrient concentration gradients that stand out as important regions for the delivery of a lateral
649 nutrient flux that dominates nutrient resupply to the subtropical gyres (Williams & Follows,
650 1998; Oschlies, 2002; Jenkins & Doney, 2003; Torres-Valdés et al., 2009; Palter et al., 2013;
651 Letscher et al., 2016; Yamamoto et al., 2019). The resolution of the BEC model employed in
652 PICO is non-eddy resolving, however it is able to simulate somewhat elevated rates of NPP (Fig.
653 1a) and associated $POC_{exp,100m}$ (Fig 4a) along these subtropical to subpolar gyre flanks at the
654 western side. These gyre recirculation region biogeochemical features are driven by a larger
655 contribution of pico-eukaryotes and diatoms to simulated NPP (Fig. 2). These regions are also
656 where PFT cellular C:P stoichiometry transitions from C-rich/P-poor stoichiometry within the
657 subtropical gyres, to more Redfield-like C:P stoichiometry poleward (Fig. 3; Fig. 4c,d). Thus, the
658 magnitude of $POC_{exp,100m}$ within the subtropical gyre recirculation regions identified as 'POC_{exp}
659 hotspots' by PICO may be sensitive to small changes to the nutrient flux stoichiometry which
660 drive cellular C:P stoichiometry. Further field-based study of the *in situ* phytoplankton
661 community composition and associated biomass C:P stoichiometry within these regions could
662 help confirm their regional 'POC_{exp} hotspot' status.

663 The PICO simulation builds from recent advances in a BEC model formulation that
664 added variable C:P stoichiometry within the three traditionally simulated PFTs (small
665 phytoplankton, diatoms, diazotrophs; Wang et al., 2019), by adding three pico-phytoplankton
666 PFTs with variable C:P stoichiometry. As compared to the variable C:P, three PFT version of the
667 BEC model (VAR-3; Wang et al., 2019), the PICO simulation exhibits ~1% higher globally
668 integrated NPP (51.4 Pg C yr^{-1} vs. 50.8 Pg C yr^{-1}) and ~18% lower $POC_{exp,100m}$ (7.0 Pg C yr^{-1} vs.
669 8.5 Pg C yr^{-1}). Thus, given that both the three and six PFT, variable C:P formulations of the BEC
670 model reproduce similarly-well, the surface to deep ocean spatial gradients in dissolved nutrient
671 concentrations (Table 2), the pico-phytoplankton enabled (6p1z) BEC model predicts similar
672 rates of NPP, with lower rates of $POC_{exp,100m}$, and lower $C:P_{exp}$ per unit of phosphorus utilized
673 within the euphotic zone as compared with the three PFT BEC model version (VAR-3; Wang et
674 al., 2019). The geographical distribution of $POC_{exp,100m}$ is similar between the PICO and VAR-3
675 simulations, however VAR-3 simulated $POC_{exp,100m}$ is approximately double to triple that
676 estimated by PICO within the subtropics to mid-latitudes (not shown), contributing to its overall
677 ~18% higher estimate of global $POC_{exp,100m}$. The lower $POC_{exp,100m}$ estimate by the PICO model
678 is likely attributable to the lower prescribed values of zooplankton grazing routed to the
679 particulate organic pool, 'graze_poc' parameter, for the pico PFTs (graze_poc = 0.07 – 0.13;
680 Table 1) versus the small phytoplankton PFT in Wang et al. (2019) (graze_poc = 0.3). Maximum
681 $C:P_{exp}$ is estimated within the ocean's subtropical gyres (Fig. 4c) in both simulations, with PICO
682 predicting slightly lower maximum $C:P_{exp}$ within the Indo-Pacific subtropics, ~140 – 145 vs.
683 ~180 in VAR-3 (not shown). PICO simulated $C:P_{exp}$ generally agrees with the spatial pattern
684 estimated from an inversion of dissolved inorganic carbon and phosphate data (Teng et al.,
685 2014), with notable differences in $C:P_{exp}$ magnitude. PICO minimum PFT C:P is set at 90 while

686 the Teng et al. (2014) inversion estimates minimum C:P_{exp} of ~60 – 100 for the equatorial and
687 subpolar regions. Maximal C:P_{exp} in the subtropical North Atlantic is ~155 in PICO compared to
688 ~355 by Teng et al. (2014). These comparisons demonstrate that estimates of the globally
689 important fluxes of marine NPP and carbon export including its C:P stoichiometry vary on the
690 order of ~10 – 50% between OBGC model formulations, highlighting the continued need for
691 observational datasets to further constrain and validate model simulations of ocean
692 biogeochemistry.

693 We are aware of two other ESMs to which addition of variable phosphorus to carbon
694 ratios within the OBGC model has been performed as well as an additional global ocean
695 biogeochemistry model. While nearly all ESMs participating in the CMIP5 suite predict
696 declining marine NPP during the 21st century (Bopp et al., 2013), the GFDL-ESM2 which runs
697 the variable C:P enabled TOPAZ2 OBGC model (Dunne, 2013), was the only ESM to predict a
698 resilient rate of marine NPP throughout this century. Presumably the mechanism at play is one in
699 which declining nutrient fluxes to the surface ocean with increasing upper ocean stratification are
700 countered by a switch in phytoplankton community composition towards smaller, more nutrient
701 plastic types and/or an increase in phytoplankton C:P that allows for maintenance of carbon
702 based NPP rates at depressed phosphorus supply fluxes. The PICO simulation presented here
703 supports this interpretation, exhibiting a marginally ~1% higher overall rate of marine NPP than
704 its analogous three PFT, Redfield C:P sister simulation (RED-3; Letscher & Moore, 2015).
705 Results from a variable C:P OBGC model that added representation of pico-phytoplankton have
706 been published (the PISCES-QUOTA model; Kwiatkowski et al., 2018). The model predicts
707 similar 21st century declines in marine NPP (–8%) and POC_{exp} (–14%) as the fixed (Redfield)
708 stoichiometry ESMs that participated in CMIP5 (Bopp et al., 2013), while noting an increase in

carbon export efficiency per unit phosphorus, which increases by 4.5%. Both the TOPAZ2 OBGC model and PISCES-QUOTA parameterize variable C:P in the phytoplankton following the optimal resource cell allocation model of Klausmeier et al., (2004), so it is surprising that the two models yield divergent predictions for 21st century marine NPP (no decline in GFDL-ESM2 using TOPAZ2, decreasing in PISCES-QUOTA), that may be due to differences in model physics and the simulated nutrient supply to the surface. The global ocean biogeochemistry modeling study of Tanioka & Matsumoto (2017) in which variable C:P stoichiometry was represented in a two phytoplankton marine ecosystem model, found that predicted declines in global export production could be mitigated by ~3% relative to a Redfield stoichiometry model over the 21st century that the authors attributed to combined mechanisms of flexible cellular nutrient to carbon ratios and regional shifts in phytoplankton community composition.

6. Future Directions

A next step with the CESM-BEC model is to perform a future climate forced simulation using PICO parameterizations to investigate changes in 21st century marine NPP and export in the context of marine phytoplankton diversity and cellular nutrient plasticity. We also wish to point out that during development of the PICO simulation it was found that the model solution was very sensitive to the choice of the grazing rates for each of the six PFTs by the single zooplankton group. This single zooplankton group formulation was not well suited to act as the top-down control on the growth of six PFTs, with the model exhibiting behavior in which it was difficult to obtain mixed communities of phytoplankton everywhere in the ocean. Future improvement of the BEC model, now carried out within the Marine Biogeochemistry Library (MARBL) in CESM v2, should include the addition of explicit nanophytoplankton groups (e.g.,

coccolithophores) and additional zooplankton groups representing multiple size classes and grazing formulations that will likely result in a more robust simulation of plankton growth, grazing, and export dynamics. Currently, a version with four zooplankton and eight phytoplankton functional types is in development (8p4z).

Acknowledgments

This work was funded by a grant from the U.S. Dept. of Energy Office of Science #DE-SC0016539 to J.K.M. and R.T.L and OCE-1848576 to A.C.M. R.T.L. also thanks discussions with members of the MARBL development team at NCAR including K. Krumhardt, M. Long, M. Levy, and K. Lindsay as well as M. Maltrud at LANL for advice during the development of the pico-phytoplankton enabled BEC-CESM. P. Flombaum at the Univ. of Buenos Aires is thanked for providing output of pico-phytoplankton biomass from predictive niche models. The authors claim no financial conflicts of interest.

Open Research

The modified BEC model source code used to generate the PICO simulation can be found on GitHub here: https://github.com/rletscher/GBC_PICO. The 20-year annually averaged output file for PICO presented in this work is available by request from the corresponding author.

References

Arrigo, K. R., Robinson, D. H., Worthen, D. L., Dunbar, R. B., DiTullio, G. R., VanWoert, M., & Lizotte, M. P. (1999). Phytoplankton community structure and the drawdown of nutrients and CO2 in the Southern Ocean. *Science*, *283*(5400), 365-367.

Aumont, O., Éthé, C., Tagliabue, A., Bopp, L., & Gehlen, M. (2015). PISCES-v2: an ocean biogeochemical model for carbon and ecosystem studies. *Geoscientific Model Development Discussions*, *8*(2).

Baer, S. E., Lomas, M. W., Terpis, K. X., Mouginot, C., & Martiny, A. C. (2017). Stoichiometry of Prochlorococcus, Synechococcus, and small eukaryotic populations in the western North Atlantic Ocean. *Environmental microbiology*, *19*(4), 1568-1583.

Behrenfeld, M. J., Boss, E., Siegel, D. A., & Shea, D. M. (2005). Carbon-based ocean productivity and phytoplankton physiology from space. *Global biogeochemical cycles*, *19*(1).

Berman-Frank, I., Quigg, A., Finkel, Z. V., Irwin, A. J., & Haramaty, L. (2007). Nitrogen-fixation strategies and Fe requirements in cyanobacteria. *Limnology and Oceanography*, *52*(5), 2260-2269.

Bopp, L., Resplandy, L., Orr, J. C., Doney, S. C., Dunne, J. P., Gehlen, M., ... & Tjiputra, J. (2013). Multiple stressors of ocean ecosystems in the 21st century: projections with CMIP5 models. *Biogeosciences*, *10*, 6225-6245.

Boyd, P. W., Strzepek, R. F., Ellwood, M. J., Hutchins, D. A., Nodder, S. D., Twining, B. S., & Wilhelm, S. W. (2015). Why are biotic iron pools uniform across high-and low-iron pelagic ecosystems?. *Global Biogeochemical Cycles*, *29*(7), 1028-1043.

Brewin, R. J., Lavender, S. J., Hardman-Mountford, N. J., & Hirata, T. (2010). A spectral response approach for detecting dominant phytoplankton size class from satellite remote sensing. *Acta Oceanol. Sin*, *29*(2), 14-32.

Britten, G. L., & Primeau, F. W. (2016). Biome-specific scaling of ocean productivity, temperature, and carbon export efficiency. *Geophysical Research Letters*, *43*(10), 5210-5216.

Brzezinski, M. A., Krause, J. W., Church, M. J., Karl, D. M., Li, B., Jones, J. L., & Updyke, B. (2011). The annual silica cycle of the North Pacific subtropical gyre. *Deep Sea Research Part I: Oceanographic Research Papers*, *58*(10), 988-1001.

Buchanan, P. J., Matear, R. J., Chase, Z., Phipps, S. J., & Bindoff, N. L. (2018). Dynamic biological functioning important for simulating and stabilizing ocean biogeochemistry. *Global Biogeochemical Cycles*, *32*(4), 565-593.

Buitenhuis, E. T., Hashioka, T., & Le Quéré, C. (2013). Combined constraints on global ocean primary production using observations and models. *Global Biogeochemical Cycles*, *27*(3), 847-858.

Buitenhuis, E. T., Li, W. K., Vaulot, D., Lomas, M. W., Landry, M. R., Partensky, F., ... & McManus, G. B. (2012). Picophytoplankton biomass distribution in the global ocean. *Earth System Science Data*, *4*(1), 37-46.

802 Cabré, A., Marinov, I., & Leung, S. (2015). Consistent global responses of marine ecosystems to
803 future climate change across the IPCC AR5 earth system models. *Climate Dynamics*, *45*(5-6),
804 1253-1280.
805
806 Casey, J. R., Lomas, M. W., Michelou, V. K., Dyhrman, S. T., Orchard, E. D., Ammerman, J.
807 W., & Sylvan, J. B. (2009). Phytoplankton taxon-specific orthophosphate (Pi) and ATP
808 utilization in the western subtropical North Atlantic. *Aquatic Microbial Ecology*, *58*(1), 31-44.
809
810 DeVries, T., & Deutsch, C. (2014). Large-scale variations in the stoichiometry of marine organic
811 matter respiration. *Nature Geoscience*, *7*(12), 890.
812
813 Dunne, J. P. (2013). Technical description of Tracers of Ocean Phytoplankton with Allometric
814 Zooplankton version 2 (TOPAZ2) used in GFDL's ESM2M and ESM2G submitted as part of the
815 Coupled Model Intercomparison Project phase 5. *J Clim. https://doi. org/10.1175/JCLI-D-12-*
816 *00150. s1*.
817
818 Dunne, J. P., Gnanadesikan, A., Sarmiento, J. L., & Slater, R. D. (2010). Technical description of
819 the prototype version (v0) of tracers of phytoplankton with allometric zooplankton (TOPAZ)
820 ocean biogeochemical model as used in the Princeton IFMIP model. *Biogeosciences*, *7*(Suppl),
821 3593.
822
823 DuRand, M. D., Olson, R. J., & Chisholm, S. W. (2001). Phytoplankton population dynamics at
824 the Bermuda Atlantic Time-series station in the Sargasso Sea. *Deep Sea Research Part II:*
825 *Topical Studies in Oceanography*, *48*(8-9), 1983-2003.
826
827 Dutkiewicz, S., Cermeno, P., Jahn, O., Follows, M. J., Hickman, A. E., Taniguchi, D. A., &
828 Ward, B. A. (2020). Dimensions of marine phytoplankton diversity. *Biogeosciences*, *17*(3), 609-
829 634.
830
831 Dyhrman, S. T., & Ruttenberg, K. C. (2006). Presence and regulation of alkaline phosphatase
832 activity in eukaryotic phytoplankton from the coastal ocean: Implications for dissolved organic
833 phosphorus remineralization. *Limnology and Oceanography*, *51*(3), 1381-1390.
834
835 Emerson, S. (2014). Annual net community production and the biological carbon flux in the
836 ocean. *Global Biogeochemical Cycles*, *28*(1), 14-28.
837
838 Fawcett, S. E., Lomas, M. W., Casey, J. R., Ward, B. B., & Sigman, D. M. (2011). Assimilation
839 of upwelled nitrate by small eukaryotes in the Sargasso Sea. *Nature Geoscience*, *4*(10), 717-722.
840
841 Flombaum, P., Gallegos, J. L., Gordillo, R. A., Rincón, J., Zabala, L. L., Jiao, N., ... & Vera, C.
842 S. (2013). Present and future global distributions of the marine Cyanobacteria Prochlorococcus
843 and Synechococcus. *Proceedings of the National Academy of Sciences*, *110*(24), 9824-9829.
844
845 Flombaum, P., Wang, W. L., Primeau, F. W., & Martiny, A. C. (2020). Global
846 picophytoplankton niche partitioning predicts overall positive response to ocean
847 warming. *Nature Geoscience*, *13*(2), 116-120.

Friedlingstein, P., Cox, P., Betts, R., Bopp, L., von Bloh, W., Brovkin, V., ... & Bala, G. (2006). Climate–carbon cycle feedback analysis: results from the C4MIP model intercomparison. *Journal of climate*, *19*(14), 3337-3353.

Galbraith, E. D., & Martiny, A. C. (2015). A simple nutrient-dependence mechanism for predicting the stoichiometry of marine ecosystems. *Proceedings of the National Academy of Sciences*, *112*(27), 8199-8204.

Garcia, H. E., Locarnini, R. A., Boyer, T. P., Antonov, J. I., Baranova, O. K., Zweng, M. M., Reagan, J. R., & Johnson, D. R. (2013). World Ocean Atlas 2013, Volume 4: Dissolved inorganic nutrients (phosphate, nitrate, silicate). S. Levitus, Ed., A. Mishonov Technical Ed., NOAA Atlas NESDIS 76, 25 pp.

Garcia, N. S., Fu, F., Sedwick, P. N., & Hutchins, D. A. (2015). Iron deficiency increases growth and nitrogen-fixation rates of phosphorus-deficient marine cyanobacteria. *The ISME journal*, *9*(1), 238.

Henson, S. A., Sanders, R., Madsen, E., Morris, P. J., Le Moigne, F., & Quartly, G. D. (2011). A reduced estimate of the strength of the ocean's biological carbon pump. *Geophysical Research Letters*, *38*(4).

Geider, R. J., & La Roche, J. (2002). Redfield revisited: variability of C [ratio] N [ratio] P in marine microalgae and its biochemical basis. *European Journal of Phycology*, *37*(1), 1-17.

Getzlaff, J., & Dietze, H. (2013). Effects of increased isopycnal diffusivity mimicking the unresolved equatorial intermediate current system in an earth system climate model. *Geophysical Research Letters*, *40*(10), 2166-2170.

Gregg, W. W., & Casey, N. W. (2004). Global and regional evaluation of the SeaWiFS chlorophyll data set. *Remote Sensing of Environment*, *93*(4), 463-479.

Hutchins, D. A., Hare, C. E., Weaver, R. S., Zhang, Y., Firme, G. F., DiTullio, G. R., ... & Trick, C. G. (2002). Phytoplankton iron limitation in the Humboldt Current and Peru Upwelling. *Limnology and Oceanography*, *47*(4), 997-1011.

Ilyina, T., Six, K. D., Segschneider, J., Maier-Reimer, E., Li, H., & Núñez-Riboni, I. (2013). Global ocean biogeochemistry model HAMOCC: Model architecture and performance as component of the MPI-Earth system model in different CMIP5 experimental realizations. *Journal of Advances in Modeling Earth Systems*, *5*(2), 287-315.

Jenkins, W. J., & Doney, S. C. (2003). The subtropical nutrient spiral. *Global Biogeochemical Cycles*, *17*(4).

892 Juranek, L. W., White, A. E., Dugenne, M., Henderikx Freitas, F., Dutkiewicz, S., Ribalet, F., ...
893 & Karl, D. M. (2020). The importance of the phytoplankton "middle class" to ocean net
894 community production. *Global Biogeochemical Cycles*, *34*(12), e2020GB006702.
895
896 Karl, D. M., Björkman, K. M., Dore, J. E., Fujieki, L., Hebel, D. V., Houlihan, T., ... & Tupas, L.
897 M. (2001). Ecological nitrogen-to-phosphorus stoichiometry at station ALOHA. *Deep Sea*
898 *Research Part II: Topical Studies in Oceanography*, *48*(8-9), 1529-1566.
899
900 Klausmeier, C. A., Litchman, E., Daufresne, T., & Levin, S. A. (2004). Optimal nitrogen-to-
901 phosphorus stoichiometry of phytoplankton. *Nature*, *429*(6988), 171.
902
903 Knapp, A. (2012). The sensitivity of marine N2 fixation to dissolved inorganic
904 nitrogen. *Frontiers in microbiology*, *3*, 374.
905
906 Kwiatkowski, L., Aumont, O., Bopp, L., & Ciais, P. (2018). The impact of variable
907 phytoplankton stoichiometry on projections of primary production, food quality, and carbon
908 uptake in the global ocean. *Global Biogeochemical Cycles*, *32*(4), 516-528.
909
910 Kwiatkowski, L., Torres, O., Bopp, L., Aumont, O., Chamberlain, M., Christian, J. R., ... &
911 Ziehn, T. (2020). Twenty-first century ocean warming, acidification, deoxygenation, and upper-
912 ocean nutrient and primary production decline from CMIP6 model
913 projections. *Biogeosciences*, *17*(13), 3439-3470.
914
915 Kwon, E. Y., Sreeush, M. G., Timmermann, A., Karl, D. M., Church, M. J., Lee, S. S., &
916 Yamaguchi, R. (2022). Nutrient uptake plasticity in phytoplankton sustains future ocean net
917 primary production. *Science Advances*, *8*(51), eadd2475.
918
919 Le Quéré, C. L., Harrison, S. P., Colin Prentice, I., Buitenhuis, E. T., Aumont, O., Bopp, L., ... &
920 Wolf-Gladrow, D. (2005). Ecosystem dynamics based on plankton functional types for global
921 ocean biogeochemistry models. *Global Change Biology*, *11*(11), 2016-2040.
922
923 Letscher, R. T., & Moore, J. K. (2015). Preferential remineralization of dissolved organic
924 phosphorus and non-Redfield DOM dynamics in the global ocean: Impacts on marine
925 productivity, nitrogen fixation, and carbon export. *Global Biogeochemical Cycles*, *29*(3), 325-
926 340.
927
928 Letscher, R. T., Moore, J. K., Teng, Y. C., & Primeau, F. (2015). Variable C: N: P stoichiometry
929 of dissolved organic matter cycling in the Community Earth System
930 Model. *Biogeosciences*, *12*(1), 209-221.
931
932 Letscher, R. T., Primeau, F., & Moore, J. K. (2016). Nutrient budgets in the subtropical ocean
933 gyres dominated by lateral transport. *Nature Geoscience*, *9*(11), 815.
934
935 Lomas, M. W., Baer, S. E., Mouginot, C., Terpis, K. X., Lomas, D. A., Altabet, M. A., &
936 Martiny, A. C. (2021). Varying influence of phytoplankton biodiversity and stoichiometric

plasticity on bulk particulate stoichiometry across ocean basins. *Communications Earth & Environment*, *2*(1), 1-10.

Lomas, M. W., Bates, N. R., Johnson, R. J., Steinberg, D. K., & Tanioka, T. (2022). Adaptive carbon export response to warming in the Sargasso Sea. *Nature Communications*, *13*(1), 1211.

Lomas, M. W., Bonachela, J. A., Levin, S. A., & Martiny, A. C. (2014). Impact of ocean phytoplankton diversity on phosphate uptake. *Proceedings of the National Academy of Sciences*, *111*(49), 17540-17545.

Lomas, M. W., Bronk, D. A., & van den Engh, G. (2011). Use of flow cytometry to measure biogeochemical rates and processes in the ocean. *Annual review of marine science*, *3*, 537-566.

Lomas, M. W., & Moran, S. B. (2011). Evidence for aggregation and export of cyanobacteria and nano-eukaryotes from the Sargasso Sea euphotic zone. *Biogeosciences*, *8*(1), 203-216.

Martiny, A. C., Hagstrom, G. I., DeVries, T., Letscher, R. T., Britten, G. L., Garcia, C. A., ... & Matsumoto, K. (2022). Marine phytoplankton resilience may moderate oligotrophic ecosystem responses and biogeochemical feedbacks to climate change. *Limnology and Oceanography*, *67*, S378-S389.

Martiny, A. C., Kathuria, S., & Berube, P. M. (2009). Widespread metabolic potential for nitrite and nitrate assimilation among Prochlorococcus ecotypes. *Proceedings of the National Academy of Sciences*, *106*(26), 10787-10792.

Martiny, A. C., Pham, C. T., Primeau, F. W., Vrugt, J. A., Moore, J. K., Levin, S. A., & Lomas, M. W. (2013a). Strong latitudinal patterns in the elemental ratios of marine plankton and organic matter. *Nature Geoscience*, *6*(4), 279.

Martiny, A. C., Vrugt, J. A., & Lomas, M. W. (2014). Concentrations and ratios of particulate organic carbon, nitrogen, and phosphorus in the global ocean. *Scientific data*, *1*(1), 1-7.

Martiny, A. C., Vrugt, J. A., Primeau, F. W., & Lomas, M. W. (2013b). Regional variation in the particulate organic carbon to nitrogen ratio in the surface ocean. *Global Biogeochemical Cycles*, *27*(3), 723-731.

Matsumoto, K., Tanioka, T., & Rickaby, R. (2020). Linkages between dynamic phytoplankton C: N: P and the ocean carbon cycle under climate change. *Oceanography*, *33*(2), 44-52.

Moore, J. K., Doney, S. C., & Lindsay, K. (2004). Upper ocean ecosystem dynamics and iron cycling in a global three-dimensional model. *Global Biogeochemical Cycles*, *18*(4).

Moore, J. K., Fu, W., Primeau, F., Britten, G. L., Lindsay, K., Long, M., ... & Randerson, J. T. (2018). Sustained climate warming drives declining marine biological productivity. *Science*, *359*(6380), 1139-1143.

983 Moore, J. K., Lindsay, K., Doney, S. C., Long, M. C., & Misumi, K. (2013). Marine ecosystem
984 dynamics and biogeochemical cycling in the Community Earth System Model [CESM1 (BGC)]:
985 Comparison of the 1990s with the 2090s under the RCP4. 5 and RCP8. 5 scenarios. *Journal of*
986 *Climate*, *26*(23), 9291-9312.
987
988 Moore, L. R., Rocap, G., & Chisholm, S. W. (1998). Physiology and molecular phylogeny of
989 coexisting Prochlorococcus ecotypes. *Nature*, *393*(6684), 464-467.
990
991 NASA Goddard Space Flight Center, Ocean Ecology Laboratory, Ocean Biology Processing
992 Group, 2018. Sea-viewing Wide Field-of-View Sensor (SeaWiFS) Ocean Color Data,
993 https://oceandata.sci.gsfc.nasa.gov/cgi/getfile/S19972472010334.L3b_CU_CHL.nc. Accessed on
994 Jun 5 2018.
995
996 Nelson, D. M., & Brzezinski, M. A. (1997). Diatom growth and productivity in an oligo-trophic
997 midocean gyre: A 3-yr record from the Sargasso Sea near Bermuda. *Limnology and*
998 *Oceanography*, *42*(3), 473-486.
999
1000 Nelson, D. M., Tréguer, P., Brzezinski, M. A., Leynaert, A., & Quéguiner, B. (1995). Production
1001 and dissolution of biogenic silica in the ocean: revised global estimates, comparison with
1002 regional data and relationship to biogenic sedimentation. *Global Biogeochemical Cycles*, *9*(3),
1003 359-372.
1004
1005 Orchard, E. D., Ammerman, J. W., Lomas, M. W., & Dyhrman, S. T. (2010). Dissolved
1006 inorganic and organic phosphorus uptake in Trichodesmium and the microbial community: The
1007 importance of phosphorus ester in the Sargasso Sea. *Limnology and Oceanography*, *55*(3), 1390-
1008 1399.
1009
1010 Oschlies, A. (2002). Nutrient supply to the surface waters of the North Atlantic: A model
1011 study. *Journal of Geophysical Research: Oceans*, *107*(C5), 14-1.
1012
1013 Palter, J. B., Marinov, I., Sarmiento, J. L., & Gruber, N. (2013). Large-scale, persistent nutrient
1014 fronts of the World Ocean: Impacts on biogeochemistry in Chemical Oceanography of Frontal
1015 Zones, p. 1-38 Springer.
1016
1017 Partensky, F., Blanchot, J., & Vaulot, D. (1999). Differential distribution and ecology of
1018 Prochlorococcus and Synechococcus in oceanic waters: a review. *Bulletin-Institut*
1019 *Oceanographique Monaco-Numero Special-*, 457-476.
1020
1021 Pasulka, A. L., Landry, M. R., Taniguchi, D. A., Taylor, A. G., & Church, M. J. (2013).
1022 Temporal dynamics of phytoplankton and heterotrophic protists at station ALOHA. *Deep Sea*
1023 *Research Part II: Topical Studies in Oceanography*, *93*, 44-57.
1024
1025 Quigg, A., Finkel, Z. V., Irwin, A. J., Rosenthal, Y., Ho, T. Y., Reinfelder, J. R., ... & Falkowski,
1026 P. G. (2003). The evolutionary inheritance of elemental stoichiometry in marine
1027 phytoplankton. *Nature*, *425*(6955), 291.
1028

Rhee, G. Y. (1978). Effects of N: P atomic ratios and nitrate limitation on algal growth, cell composition, and nitrate uptake. *Limnology and oceanography*, *23*(1), 10-25.

Richardson, T. L., & Jackson, G. A. (2007). Small phytoplankton and carbon export from the surface ocean. *Science*, *315*(5813), 838-840.

Séférian, R., Berthet, S., Yool, A., Palmieri, J., Bopp, L., Tagliabue, A., ... & Yamamoto, A. (2020). Tracking improvement in simulated marine biogeochemistry between CMIP5 and CMIP6. *Current Climate Change Reports*, *6*(3), 95-119.

Sharoni, S., & Halevy, I. (2020). Nutrient ratios in marine particulate organic matter are predicted by the population structure of well-adapted phytoplankton. *Science Advances*, *6*(29), eaaw9371.

Shire, D. M., & Kustka, A. B. (2015). Luxury uptake, iron storage and ferritin abundance in Prochlorococcus marinus (Synechococcales) strain MED4. *Phycologia*, *54*(4), 398-406.

Siegel, D. A., Buesseler, K. O., Doney, S. C., Sailley, S. F., Behrenfeld, M. J., & Boyd, P. W. (2014). Global assessment of ocean carbon export by combining satellite observations and food-web models. *Global Biogeochemical Cycles*, *28*(3), 181-196.

Silsbe, G. M., Behrenfeld, M. J., Halsey, K. H., Milligan, A. J., & Westberry, T. K. (2016). The CAFE model: A net production model for global ocean phytoplankton. *Global Biogeochemical Cycles*, *30*(12), 1756-1777.

Smith, R., Jones, P., Briegleb, B., Bryan, F., Danabasoglu, G., Dennis, J., ... & Hecht, M. (2010). The parallel ocean program (POP) reference manual: ocean component of the community climate system model (CCSM) and community earth system model (CESM). *Rep. LAUR-01853*, *141*, 1-140.

Sohm, J. A., Ahlgren, N. A., Thomson, Z. J., Williams, C., Moffett, J. W., Saito, M. A., ... & Rocap, G. (2016). Co-occurring Synechococcus ecotypes occupy four major oceanic regimes defined by temperature, macronutrients and iron. *The ISME journal*, *10*(2), 333-345.

Sohm, J. A., & Capone, D. G. (2006). Phosphorus dynamics of the tropical and subtropical north Atlantic: Trichodesmium spp. versus bulk plankton. *Marine Ecology Progress Series*, *317*, 21-28.

Stawiarski, B., Buitenhuis, E. T., & Fallens, M. (2018). The physiological response of seven strains of picophytoplankton to light, and its representation in a dynamic photosynthesis model. *Limnology and Oceanography*, *63*(S1), S367-S380.

Stukel, M., Coles, V., Brooks, M., & Hood, R. (2014). Top-down, bottom-up and physical controls on diatom-diazotroph assemblage growth in the Amazon River plume. *Biogeosciences*, *11*(12).

1075 Stukel, M. R., Décima, M., Selph, K. E., Taniguchi, D. A., & Landry, M. R. (2013). The role of
1076 Synechococcus in vertical flux in the Costa Rica upwelling dome. *Progress in*
1077 *Oceanography*, *112*, 49-59.
1078
1079 Stukel, M. R., & Landry, M. R. (2010). Contribution of picophytoplankton to carbon export in
1080 the equatorial Pacific: A reassessment of food web flux inferences from inverse
1081 models. *Limnology and Oceanography*, *55*(6), 2669-2685.
1082
1083 Tagliabue, A., Mtshali, T., Aumont, O., Bowie, A. R., Klunder, M. B., Roychoudhury, A. N., &
1084 Swart, S. (2012). A global compilation of dissolved iron measurements: focus on distributions
1085 and processes in the Southern Ocean. *Biogeosciences*, *9*(6).
1086
1087 Tanioka, T., & Matsumoto, K. (2017). Buffering of ocean export production by flexible
1088 elemental stoichiometry of particulate organic matter. *Global Biogeochemical Cycles*, *31*(10),
1089 1528-1542.
1090
1091 Tanioka, T., & Matsumoto, K. (2020). A meta-analysis on environmental drivers of marine
1092 phytoplankton C: N: P. *Biogeosciences*, *17*(11), 2939-2954.
1093
1094 Teng, Y. C., Primeau, F. W., Moore, J. K., Lomas, M. W., & Martiny, A. C. (2014). Global-scale
1095 variations of the ratios of carbon to phosphorus in exported marine organic matter. *Nature*
1096 *Geoscience*, *7*(12), 895.
1097
1098 Timmermans, K. R., Van der Wagt, B., Veldhuis, M. J. W., Maatman, A., & De Baar, H. J. W.
1099 (2005). Physiological responses of three species of marine pico-phytoplankton to ammonium,
1100 phosphate, iron and light limitation. *Journal of sea research*, *53*(1-2), 109-120.
1101
1102 Torres-Valdés, S., Roussenov, V. M., Sanders, R., Reynolds, S., Pan, X., Mather, R., ... &
1103 Williams, R. G. (2009). Distribution of dissolved organic nutrients and their effect on export
1104 production over the Atlantic Ocean. *Global Biogeochemical Cycles*, *23*(4).
1105
1106 Van Mooy, B. A., Fredricks, H. F., Pedler, B. E., Dyhrman, S. T., Karl, D. M., Koblížek, M., ...
1107 & Webb, E. A. (2009). Phytoplankton in the ocean use non-phosphorus lipids in response to
1108 phosphorus scarcity. *Nature*, *458*(7234), 69-72.
1109
1110 Vaulot, D., Gall, F. L., Marie, D., Guillou, L., & Partensky, F. (2004). The Roscoff Culture
1111 Collection (RCC): a collection dedicated to marine picoplankton. *Nova Hedwigia*, *79*(1-2), 49-
1112 70.
1113
1114 Wang, W. L., Moore, J. K., Martiny, A. C., & Primeau, F. W. (2019). Convergent estimates of
1115 marine nitrogen fixation. *Nature*, *566*(7743), 205-211.
1116
1117 Weber, T. S., & Deutsch, C. (2010). Ocean nutrient ratios governed by plankton
1118 biogeography. *Nature*, *467*(7315), 550.
1119

Westberry, T., Behrenfeld, M. J., Siegel, D. A., & Boss, E. (2008). Carbon-based primary productivity modeling with vertically resolved photoacclimation. *Global Biogeochemical Cycles*, *22*(2).

Williams, R. G., & Follows, M. J. (1998). The Ekman transfer of nutrients and maintenance of new production over the North Atlantic. *Deep Sea Research Part I: Oceanographic Research Papers*, *45*(2-3), 461-489.

Wilson, J. D., Andrews, O., Katavouta, A., de Melo Viríssimo, F., Death, R. M., Adloff, M., ... & Ying, R. (2022). The biological carbon pump in CMIP6 models: 21st century trends and uncertainties. *Proceedings of the National Academy of Sciences*, *119*(29), e2204369119.

Yamamoto, A., Palter, J. B., Dufour, C. O., Griffies, S. M., Bianchi, D., Claret, M., ... & Galbraith, E. D. (2018). Roles of the Ocean Mesoscale in the Horizontal Supply of Mass, Heat, Carbon, and Nutrients to the Northern Hemisphere Subtropical Gyres. *Journal of Geophysical Research: Oceans*, *123*(10), 7016-7036.